Stellar population and metal production in AGN discs

Chris L. Fryer,[1]* Jiamu Huang [ORCID],[2] Mohamad Ali-Dib,[3] Amaya Andrews,[1] Zhenghao Xu[2]
and Douglas N. C. Lin[4]

[1] *Los Alamos National Laboratory, Los Alamos, NM 87545, USA*
[2] *Department of Physics, University of California, Santa Barbara, CA 93106, USA*
[3] *Center for Astrophysics and Space Science (CASS), New York University Abu Dhabi, PO Box 129188, UAE*
[4] *Department of Astronomy and Astrophysics, University of California, Santa Cruz, CA 95064, USA*

ABSTRACT

As gravitational wave detections increase the number of observed compact binaries (consisting of neutron stars or blacks), we begin to probe the different conditions producing these binaries. Most studies of compact remnant formation focus either on stellar collapse from the evolution of field binary stars in gas-free environments or on the formation of stars in clusters where dynamical interactions capture the compact objects, forming binaries. But a third scenario exists. In this paper, we study the fate of massive stars formed, accrete gas, and evolve in the dense discs surrounding supermassive black holes. We calculate the explosions produced and compact objects formed by the collapse of these massive stars. Nucleosynthetic yields may provide an ideal, directly observable, diagnostic of the formation and fate of these stars in active galactic nuclei. We present a first study of the explosive yields from these stars, comparing these yields with the observed nucleosynthetic signatures in the discs around supermassive stars with quasars. We show that, even though these stars tend to form black holes, their rapid rotation leads to discs that can eject a considerable amount of iron during the collapse of the star. The nucleosynthetic yields from these stars can produce constraints on the number of systems formed in this manner, but further work is needed to exploit variations from the initial models presented in this paper.

Key words: stars: massive – supernovae: general – (galaxies:) quasars: general – (stars:) gamma-ray burst: general.

1 INTRODUCTION

Our understanding of compact remnants (black holes and neutron stars) and their formation mechanisms has increased in the past few years due to a rapidly growing set of gravitational wave observations probing the properties (masses and spins) of these compact objects (Abbott et al. 2019, 2021, 2023, 2024). Most studies of the remnant formation have focused on field star evolution (e.g. Fryer, Woosley & Hartmann 1999; Belczyński, Bulik & Zbijewski 2000; Kruckow et al. 2018; Belczynski et al. 2020; Broekgaarden et al. 2021; Romagnolo et al. 2023). Other formation scenarios have been considered including star formation (and mergers) in dense stellar clusters (Rodriguez, Chatterjee & Rasio 2016; Rastello et al. 2020; Britt et al. 2021) and star formation in extreme conditions such as in the discs of active galactic nuclei (AGNs; Paczynski 1978; Eldridge & Stanway 2016; Yang et al. 2019; Zevin et al. 2021; Mandel & Broekgaarden 2022; Stevenson & Clarke 2022; Arca Sedda, Naoz & Kocsis 2023; Kritos et al. 2024; McKernan & Ford 2024). To fully analyse this growing set of binary compact remnant observations, we must understand all of the potential formation scenarios of neutron stars and black holes.

One of the least-studied formation scenarios is the evolution and collapse of massive stars in AGN discs. The conditions in the standard

α-disc prescription of the accretion discs around a supermassive black hole (SMBH) with masses between 10^6 and $10^8 M_\odot$ are such that the disc is susceptible to gravitational instabilities (Paczynski 1978). These instabilities, in turn, can drive the formation of stars within the disc. Star formation in AGN discs has been studied for over two decades (Goodman 2003; Goodman & Tan 2004; Thompson, Quataert & Murray 2005; Chen et al. 2023). AGN discs also capture mature stars in the nuclear clusters surrounding the central SMBHs (Artymowicz, Lin & Wampler 1993; Davies & Lin 2020; MacLeod & Lin 2020).

The evolution of these stars has recently been numerically modelled using the MESA scheme (Cantiello, Jermyn & Lin 2021; Jermyn et al. 2022; Ali-Dib & Lin 2023). The fact that these stars form immersed in a dense disc causes them to evolve very differently than field stars. The relatively high densities surrounding these stars cause them to accrete mass until the star, no matter its starting mass, exceeds a mass of a few hundred $M_\odot$. This high mass then drives mass-loss when the star reaches its Eddington luminosity (Ali-Dib & Lin 2023).

In this paper, we calculate the further evolution and final fate of these peculiar stars. We assess both their potential for driving supernova-like explosions and the properties of the compact remnants formed in their collapse. One way to test the formation rate and final fate of these stars is to study the nucleosynthetic yields from these stars (Huang, Lin & Shields 2023). With our explosion

* E-mail: fryer@lanl.gov

calculations we can calculate the detailed yields from these AGN disc stars, combining the yields from the stellar winds and the collapse-driven explosions. We then compare the predicted yields to those observed in AGN discs.

The outline of the paper is as follows. We first review the evolution of the AGN-disc stars used in this study (Section 2). Using the structures (e.g. density, temperature, composition profiles) from the stellar models described in Section 2, we then determine the fate of these stars (remnant formation and explosion properties), leveraging current analyses of the collapse of field stars (Section 3). The yields (combining yields ejected in stellar winds, material processed in disc formed around the collapsed star, and the stellar material ejected by the disc wind) from the stellar collapse are discussed in Section 4. These yields are compared to observations of AGN discs in quasar systems in Section 5. We conclude with a summary of our results and a discussion of future work.

2 STELLAR EVOLUTION IN AGN DISCS

Stellar evolution in the dense environments of AGN discs proceeds very differently than that of field stars. The dense circumstellar AGN disc material leads to continued accretion onto the star. Independent of their initial mass, these AGN-disc stars can acquire up to several hundred solar masses before they efficiently shed mass through intense stellar winds. If the accreted material in the envelope is well mixed with the He ashes in the nuclear-burning (through CNO cycle) core, this 'metabolic' process would enable the massive stars embedded in the dense inner regions of AGN discs to indefinitely remain on the main sequence (Cantiello et al. 2021). However, if their radiative zone provides an effective buffer to prevent significant mixing, the He and N abundances in these stars' core would increase through the CNO cycle on the main sequence. Consequently, their mass–luminosity function would evolve and their Eddington limit would be marginally maintained by shedding envelope mass with net enhanced He and N yields. After nearly all the H content is exhausted in their cores and a major fraction of their total mass is lost, these stars undergo post-main-sequence evolution. Subsequently, they release several $M_\odot$ of He and C + O-enriched yields before their evolution calculation with the MESA code is halted at the onset of Si burning (Ali-Dib & Lin 2023). Shortly thereafter, the Mg and Si-laden cores collapse. In this paper, we consider the possibility of type II supernovae resulting from the core collapse and determine their yields of iron peak elements. For this first study of the compact remnants, explosions and yields from these massive stars, we simulate stellar evolution varying the rotational velocity, the metallicity, and the AGN disc density (corresponding to different positions in the AGN disc).

Our main-sequence and post-main-sequence stellar evolution models essentially follow the prescription outlined in Cantiello et al. (2021). We adopt the modification made by Ali-Dib & Lin (2023) by switching off the 'extra mixing' in the radiative zones which was implemented by Cantiello et al. (2021) to enable the replenishment of freshly accreted H-rich gas to the core where the conversion of H to He through the CNO cycle is ongoing. We initiate a simulation with a young stellar object with a mass $M_{\rm initial} = 1\,{\rm M_\odot}$ embedded in an AGN disc with nominal boundary conditions $\rho_{\rm disc} = 6 \times 10^{-17}$ g cm^{-3} and sound speed $c_{s_{\rm disc}} = 10^6$ cm s^{-1}. The star initially grows through Bondi accretion. As the star's mass increases above roughly a few hundred $M_\odot$, its luminosity rapidly approaches the Eddington limit with an intensifying radiation-pressure driven wind.

We model this wind following Cantiello et al. (2021) as a super-Eddington outflow at the escape velocity with a mass-loss rate set by

the excess luminosity and defined as

$$\dot{M}_{\rm Edd} = -\frac{L_*}{v_{\rm esc}^2}\left[1 + \tanh\left(\frac{L_* - L_{\rm Edd}}{0.1 L_{\rm Edd}}\right)\right], \qquad (1)$$

where the tanh term is to help numerical convergence.

A balance between the accretion and wind mass-loss rates is established with a mass $M_{\rm eq} \sim 630\,{\rm M_\odot}$. We take into account the partial retention of the He-laden wind and the local recycling of the accreted gas due to the inflow–outflow congestion (Chen et al. 2024). Provided there is no 'extra' rotational mixing, the presence of a radiative envelope in main-sequence stars maintains a barrier which cuts off the H replenishment to the nuclear furnace. As He increases with H depletion in its isolated core, the star brightens and the state of marginal Eddington-limited equilibrium is maintained through the radiation-driven mass reduction. In comparison with the disc gas, the gas released by the main sequence stars carries excess He and N yields with slightly C + O depletion (because the C + N + O abundance is conserved through the CNO burning). After the H abundance vanishes in its core, the star's mass is reduced to ~ 25–$30\,{\rm M_\odot}$ and it transitions to post-main-sequence evolution with the onset of He burning. For a more detailed description of the approaches, we refer the reader to the work of Cantiello et al. (2021) on the immortal and Ali-Dib & Lin (2023) on the metamorphic stars.

Our previous models neglect the effect of stellar rotation. In principle, the freshly accreted H-rich gas may pass through the radiative envelope via meridional circulation and mix with the He-ashes-laden gas in the core. But, unless the star is spinning at a large fraction of the break-up rate, limited elemental diffusion cannot sufficiently replenish the hydrogen fuel to significantly prolong the CNO cycle on the main sequence. Carrying a maximum amount of Keplerian specific angular momentum at the stellar surface, the accreted gas is supplied by the gravito-turbulent eddies in AGN discs. On scales up to the disc thickness (larger than the star's Bondi radius), the eddies' spin vector sporadically re-orients on their turn-over time-scale (comparable to the disc's orbital time-scale $\tau_{\rm eddy} = \Omega^{-1}$). Over the much longer characteristic accretion time-scale ($M_\star/\dot{M}_\star$), the stochastic accretion from the randomly aligned eddies reduces the net angular-momentum deposition on to the star well below its rotational break-up range (Chen & Lin 2023). Moreover, angular momentum may be removed from the star by its outflowing wind due to the coupling between different regions of the stellar interior by convection or magnetic fields.

Based on these considerations, we neglect the effect of stellar spin in inducing 'extra' rotational mixing during AGN stars' main-sequence evolution. However, during the star's brief post-main-sequence evolution, there are three effects which can significantly boost angular momentum acquisition – especially during the supergiant phase when its mass has reduced to $M_\star \lesssim 25$–$30\,{\rm M_\odot}$, shock radius $R_{\rm rot}$ to $\sim 2\,{\rm R_\odot}$, and its photosphere radius has expanded to $R_{\rm ph,rot} \sim 10^2\,{\rm R_\odot}$. First, with a rotational velocity $v_{\rm rot}$ comparable to the Keplerian speed at $R_{\rm ph,rot}$, $v_{\rm rot} \sim V_{\rm Kep}(R_{\rm ph,rot}) \sim 200$ km s$^{-1} \sim 0.1 V_{\rm Kep}(R_{\rm rot})$ and the specific angular momentum $j_\star \simeq (GM_\star R_{\rm rot})^{1/2} \sim 2 \times 10^{19}$ cm s^{-1} on the star's shock radius. Secondly, the stellar envelope is fully convective. Although H, He, and heavy elements are well mixed even without any rotational effects, the accretion rate of disc gas is inadequate to replenish either H or He to slow-down the star's post-main-sequence evolution. Finally, the star's evolution time-scale is reduced to $\sim 10^{3-4}$ yr which is comparable to the turnover time-scale $\tau_{\rm eddy}$ of gravito-turbulent eddies (which is comparable to the star's orbital period around the SMBH). Thereafter, the accreted gas has no time to undergo spin reorientation and the rotation speed of the star $v_{\rm rot}$ may have

Table 1. Stellar models with AGN-disc accretion. The total pre-collapse stellar mass M_{fi} is mostly that M_{CO} of C and O. The silicon core is the region where the silicon mass fraction is greater than 10 per cent. It contains a mass M_{Si}.

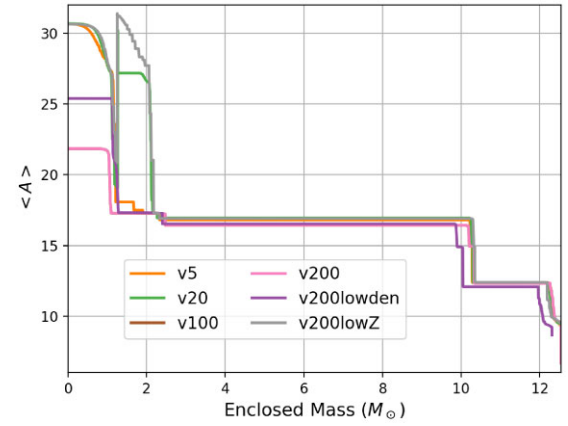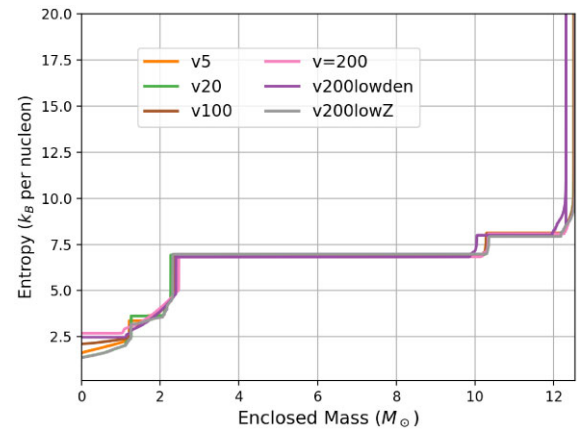| Model	M_{rot} $(M_\odot)$	v_{rot} $(10^7 \, cm \, s^{-1})$	R_{rot} $(R_\odot)$	J_{rot} $(10^{52} \, g \, cm^2 \, s^{-1})$	$M_{fi} \simeq M_{CO}$ $(M_\odot)$	M_{Si} $(M_\odot)$	R_{fi} $(R_\odot)$	$R_{ph,fi}$ $(R_\odot)$	J_{fi} $(10^{52} \, g \, cm^2 \, s^{-1})$
v5	25	0.05	1.28	0.014	12.5	1.9	0.38	303.4	0.0045
v20	25	0.2	1.28	0.060	12.5	2.1	0.39	303.4	0.018
v100	25	1	1.28	0.29	12.3	1.3	0.37	304.04	0.089
v200	25	2	1.29	0.59	12.5	1.1	0.36	305.6	0.18
v200lowZ	29	2	1.39	1.71	12.5	2.2	0.38	306.1	0.219
v200lowden	30	2	1.34	4.38	12.3	1.3	0.39	8.41	0.498

magnitudes range from negligible to small, $\sim \mathcal{O}(0.1)$, fraction of $v_{Kep}(R_{rot})$. In principle, super Keplerian rotation speed may also be temporarily established near the star's surface after some extreme merger events (Chen & Lin 2024) although it would rapidly spin-down through intense mass and angular momentum losses.

A non-negligible amount of spin angular momentum for the post-main-sequence stars introduces the possibility of disc formation around compact remnants of collapse core (Section 3). In order to take these effects into account, we consider a range of rotation speed v_{rot} on the stellar surface. We utilize the new_surface_rotation_v and adjust_J_q_limit flags in the MESA code to compute the star's internal specific angular momentum distribution for these outer boundary conditions. For the fiducial models (v5, v20, v100, and v200), we adopt solar composition for the disc gas. We also include additional variations (v200lowden and v200lowZ) for low disc density ($= 10^{-17}$ g cm^{-3}) and purely H and He gas supply (Cantiello et al. 2021) in the v200lowden and v200lowZ models, respectively. A comprehensive evaluation of the star's most likely rotational properties will be examined elsewhere.

With mass $M_\star = M_{rot} = 25–30 \, M_\odot$, shock radius $R_{rot} \sim R_\odot$ (equation 33 in Cantiello et al. 2021), radius of photosphere $R_{ph,rot} \simeq 120 \, R_\odot$, rotation speed at the stellar surface $v_{rot} = 5–200$ km s^{-1} (ranging negligible to modest fraction of v_{Kep}), and total angular momentum J_{rot} (Table 1), we relax the rotational models subjected to the influence of magnetic coupling to obtain the angular momentum distribution within R_{rot} (Paxton et al. 2013) at the end of main sequence of evolution. We continue the MESA calculation of the star's post-main-sequence evolution until the onset of Si burning. We use the standard MESA algorithm to compute the evolution of star's angular momentum and composition distribution. Radiation-pressure driven mass-loss (mostly in He, C, and O; Ali-Dib & Lin 2023) along with angular momentum removal, enables the star's luminosity to be maintained at a marginal Eddington-limited level.

The MESA calculation is terminated at the onset of Si burning with a temperature $10^{9.5}$ K before the core collapse. The star has a mass $M_{fi} = 12 \, M_\odot$, a radius R_{fi}, and a total angular momentum J_{fi} (Table 1). In all models, C and O contribute to most of the mass and a modest mass $M_{Si} \sim 1–2 \, M_\odot$ at the centre of the pre-collapsing core have > 10 per cent concentration of Silicon (Fig. 1). Only a negligible fraction of Si and Mg yield is released to the disc before the collapse. The corresponding entropy profiles are shown in Fig. 2. Just as with the abundances, there is very little variation in entropy in these models. The amount of mass reduction ($M_{fi}/M_{rot} \sim 0.5$) does not depend on v_{rot} which indicates that the mass-loss is mostly driven by radiation pressure, not by centrifugal force.

Within the shock radius R_{fi} (Cantiello et al. 2021), much smaller than the photospheric radius $R_{ph,fi}$, there are noted differences in the specific angular momentum distribution (Fig. 3) between the three rotational models (with surface $v_{rot} = 5$, 20, and 200 km s^{-1}

Figure 1. Average atomic mass of our stars at collapse as a function of the enclosed mass coordinate. We vary the rotation speed to include outer star spin-up from 5 to 200 km s^{-1}. We also include a model with embedded in a lower metallicity disc and a model at lower metallicity – see Table 2. The variation in the inner $2 \, M_\odot$ is due to slight differences in the final time dump of the simulations as the material is burning to silicon. The sharp jumps in abundances at $1 \, M_\odot$ occur at the dividing line between core and shell C/O burning. As we evolve the star further, these abundances would become more smooth. Beyond those differences, the models are very similar. This is because, in all models, the stars accrete material until they achieve the same high mass before losing most of the mass through winds. In our case, the wind mass-loss is not metallicity-driven as the Eddington luminosity is set by the electron scattering opacity. These stars end up with very large O cores that will collapse to black holes in all supernova models.

Figure 2. Entropy versus enclosed mass for the same suite of models as Fig. 1/Table 2. The entropy of all our stars are nearly identical.
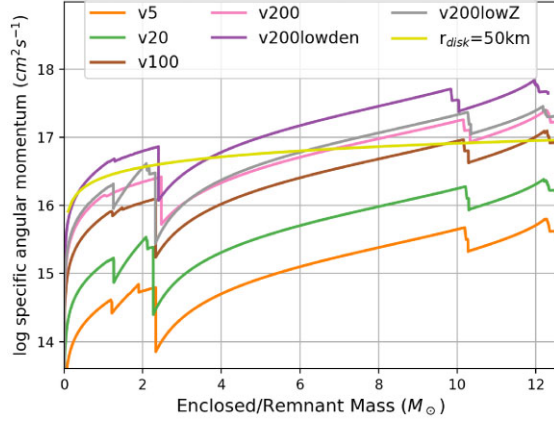
Figure 3. Specific angular momentum profiles for the models described in Table 2. High angular momenta are needed to form a disc with a radius of 50 km. For comparison, the angular momentum needed to form a $r_{disc} \simeq 50$ km disc is plotted as a function of the compact remnant mass M_{rem} set to the enclosed mass ($r_{disc} > r_{ISCO}$, equations 4 and 5). Only our models with initial rotation velocities above $200 \, \mathrm{km \, s^{-1}}$ have sufficiently high angular momenta to form a disc.

in Table 1). One major uncertainty in the MESA models (Paxton et al. 2013) is the efficiency of angular momentum transfer between different layers of the envelope and convective/radiative interface (due to transition in the composition in Fig. 1). Magnetic breaking by the stellar wind on star's surface and the evolution of internal density distribution (changes in the envelope size) can lead to differential rotation. In principle, strong coupling can re-establish uniform rotation with specific angular momentum proportional to the square of distance from the stellar core. Here, we use the standard MESA prescription for partial angular-momentum diffusion between layers with different composition. At interfaces where convection is stabilized by molecular weight gradient there are significant drops in the angular velocity (Fig. 3). The difference between $M_{rot}/M_{fi} \sim 2$ and $J_{rot}/J_{fi} \sim 3$ for models v5, v20, and v200 (also between $M_{rot}/M_{fi} \sim 2$ and $J_{rot}/J_{fi} \sim 8$ for the v200lowZ and v200lowden models in Table 1) is a manifestation of a modest amount of magnetic breaking imposed by the wind.

3 STELLAR COLLAPSE: REMNANT MASSES, EJECTA PROPERTIES, AND GRAVITATIONAL WAVES

Although we do not, and cannot, follow the evolution of the stars to collapse, we can infer their fate based on the structure near carbon exhaustion and the onset of Si burning with the MESA models. A number of prescriptions exist to determine the compact remnant produced in stellar collapse (Fryer et al. 2012; Fryer, Olejak & Belczynski 2022). For all of these prescriptions, we do not expect a supernova explosion (even a weak supernova explosion) for slowly or non rotating stars with CO core masses (M_{CO}) $\geq 8 \, M_{\odot}$ at the onset of Si burning. As shown in Table 1 and Fig. 1, all of the stars produced in AGN discs produce CO cores above this mass. We expect the residual core of these stars to collapse and form black holes.

In the absence of a sufficiently large spin angular momentum, these stars are unlikely to eject much mass during the collapse. Under this condition, the remnant's mass would equal the mass of the collapsing star and the yields would be limited to the stellar-wind mass-loss from the star (in elements lighter than Si) during their main sequence and post-main-sequence evolution (Ali-Dib & Lin 2023). In this section,

we focus on the mass ejection from discs formed in the collapse of rotating stars.

3.1 Formation of discs around remnant black holes

As we have discussed above, AGN stars likely to spin up at the end of their post-main-sequence evolution as they exchange mass with the disc around the SMBH. For our progenitors, the fast-spinning model (with $v_{rot} = 200 \, \mathrm{km \, s^{-1}}$) has sufficient angular momentum to produce a disc outside the remnant's gravitational radius during the collapse. We focus on this type of progenitors for our study.

The initial collapsing material (from the central region of the core) forms the black hole. At first, the angular momentum is too low to significantly impede the infall and the imploding stellar material passes through the event horizon, adding momentum and mass to the remnant. Even if the compact remnant is a neutron star, at these accretion rates, neutrino cooling rapidly removes the entropy from the material piling up on the neutron star and it quickly compresses becoming part of the remnant (Fryer, Benz & Herant 1996). As the outer, higher angular-momentum material falls onto the compact remnant, centrifugal forces cause it to stall and accumulate in the disc. It is believed that viscous heating in the disc drives winds that eject both mass and angular momentum (see review in Kaltenborn et al. 2023). As the material in the disc loses angular momentum, it moves inward. In our model, the angular momentum deposited onto the black hole by this disc material is limited to its angular momentum at the event horizon.

The imploding star either accretes on to the compact object or, for sufficiently high angular momentum material, feeds the disc at roughly the free-fall time (Fryer et al. 1996). The accretion rate/disc-feeding rate ($\dot{M}_{disc}$) can be determined using the stellar structure:

$$\dot{M}_{disc} = \Delta M / \Delta t_{ff} = (M_{k+1} - M_k)/(t_{ff_{k+1}} - t_{ff_k}), \quad (2)$$

where M_k is the enclosed mass at the radial coordinate r_k and t_{ff_k} is the free-fall time at that coordinate:

$$t_{ff_k} = \pi r_k^{1.5}/(2GM_{BH_k})^{1/2} \quad (3)$$

where G is the gravitational constant and M_{BH_k} is the black hole mass. $M_{BH_k} \approx M_k$ but will be slightly smaller due to wind mass-loss (we include this mass-loss in our calculations). For low angular momentum material, this is the accretion rate on to the black hole. Conservation of angular momentum allows us to set the position of the disc (r_{disc}):

$$r_{disc} = j_k^2/(GM_{BH_k}), \quad (4)$$

where j_k is the specific angular momentum in the star at position k. If r_{disc} is greater than the radius of the innermost stable orbit (r_{ISCO}), a disc is formed. We assume the prograde calculate of r_{ISCO}:

$$r_{ISCO} = GM_{k+1}/c^2(3 + Z_2 - \sqrt{(3 - Z_1)(3 + Z_1 + 2Z_2)}), \quad (5)$$

where $Z_1 = 1 + \sqrt[3]{1 - \chi^2}(\sqrt[3]{1 + \chi^2} + \sqrt[3]{1 - \chi^2})$, $Z_2 = \sqrt{3\chi^2 + Z_1^2}$ and $\chi = cJ_{BH_k}/(GM_{BH_k}^2)$ are dimensionless parameters, J_{BH_k} is the total angular momentum of the black hole when material at coordinate k is in the disc. Our models with initial rotation velocities above $100 \, \mathrm{km \, s^{-1}}$ have sufficiently high angular momenta to form a disc (Fig. 3). Since the accretion time through a compact disc (assuming an α-disc) (Shakura & Sunyaev 1973) is typically shorter than the infall time from R_{fi}, we can estimate the accretion rate on to the black hole as a function of time for our stellar models (Fig. 4).
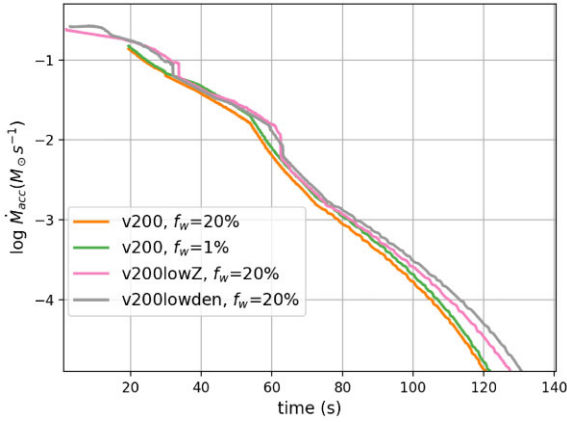
Figure 4. Accretion rate onto the black hole as a function of time for the models described in Table 2 using the free-fall time of the collapsing stellar material (equation 3) and an $\alpha = 0.01$ accretion disc (Deng, Mayer & Latter 2020) These accretion rates are similar to those seen in higher-mass collapsar models (Popham, Woosley & Fryer 1999).
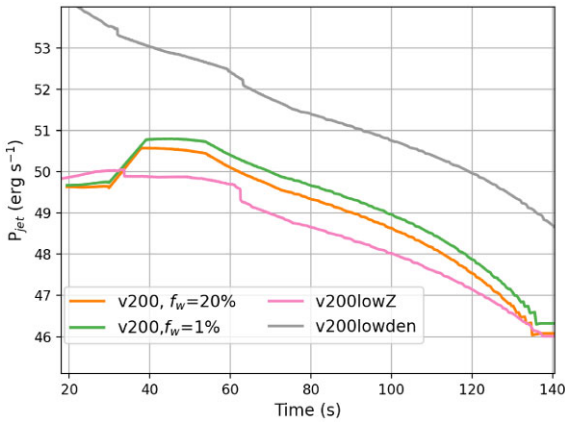

Figure 5. Power of the jet (equation 6) as a function of time for the models in Table 2. The accretion discs produced powerful jets that can reproduce the most powerful GRBs observed. But these jets will have to propagate through the AGN disc and will be far more baryon-loaded than normal GRBs. It is possible that these jets will eject the stellar material as the pressure wave in the jet wraps around the star.

3.2 Outflow from the disc

The disc formed in this implosion can power outflows, both through a magnetic-dynamo driven jet (Popham et al. 1999) and viscosity-driven winds (also probably due to magnetic field processes). Although neither of these outflows are fully understood, current simulations, analyses and observations all provide some insight into the behaviour of these outflows. For the jet power for our models, we use the results from Heger et al. (2003):

$$P_{\text{jet}} = 10^{50} a_{\text{spin}}^2 10^{0.1/(1-a_{\text{spin}})-0.1} \left(\frac{M_{\text{BH}}}{3\,M_\odot} \right)^{-3} \frac{\dot{M}_{\text{disc}}}{0.1\,M_\odot\,\text{s}^{-1}}\,\text{erg s}^{-1}, \quad (6)$$

where M_{BH}, a_{spin} are the black hole mass and spin, respectively, $\dot{M}_{\text{disc}}$ is the accretion rate. Other models argue for a much stronger jet (Gottlieb et al. 2023). Fig. 5 shows the jet power using equation (6) as a function of time since the formation of the disc and hence jet. The high angular momentum in the low-density model produces a rapidly spinning black hole and early disc formation. Under our jet power prescription, this produces a very powerful jet.
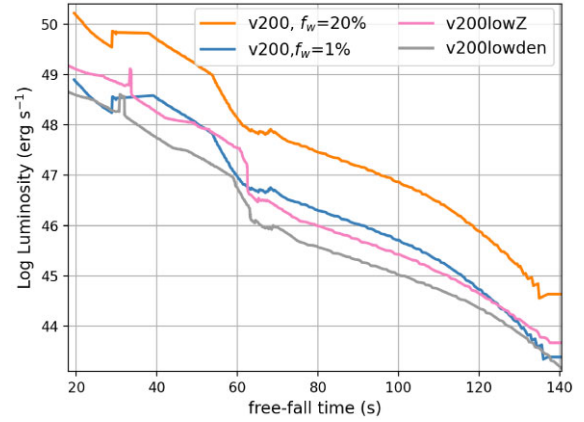

Figure 6. Power of the wind outflows assuming 20 per cent of the disc mass is ejected with an excess energy set to 1/2 the escape velocity. These winds will further contribute to ejecting the star.

Table 2. MESA final mass of the remnant (M_{remnant}), amount of mass processed through the disc (M_{disc}), total amount of energy released by the jet (E_{jet}), and from the disc wind ($E_{\text{disc-wind}}$) inferred from our collapse models.

Model	M_{remnant} ($M_\odot$)	M_{disc} ($M_\odot$)	E_{jet} (10^{52} erg)	$E_{\text{disc-wind}}$ (10^{49} erg)
v5	12.5	0	0	0
v20	12.5	0	0	0
v100	12.5	0	0	0
v200	11.7	7.7	1–2	50–100
v200lowZ	11.9	6.0	0.25–0.5	5–10
v200lowden	11.3	9.3	500–1000	5–10

The jet sweeps up very little mass ($< 10^{-4}\,M_\odot$) and, in of itself, it does not alter the final remnant mass. But as the jet punches through the star, it drives a pressure wave that can eject the outer layers of the star (MacFadyen & Woosley 1999). Some fraction of the jet energy is converted into this pressure wave, driving an explosion (we assume 10 per cent of the jet power goes into driving this pressure wave).

The accretion disc itself drives an outflow whose mass is predicted to be anywhere between 1 and 30 per cent of the disc mass (Kaltenborn et al. 2023). For our yields models, we assume that 20 per cent of the disc mass is ejected. We assume that the wind ejecta is uniform across the extent of the disc and the ejecta velocity is set to 1/2 of the escape velocity. Because these outflows have more mass, they produce a more powerful explosion (Fig. 6) and lower-mass black holes (Table 2).

3.3 From neutron star to black hole cores

In stellar collapse, the core initially forms a neutron star. In our models, the accretion rate is high and this proto-neutron star ultimately collapses to a black hole (within a few seconds). This short-lived neutron-star phase can be probed by the thermal neutrino and gravitational wave emission. As with normal stellar-collapse, the neutrino and gravitational wave signal is limited to events in the Milky Way. For the collapse of a rotating core, the fate depends on a parameter $\beta \equiv T/|W|$, where T is the rotational energy and $|W|$ is the absolute value of the gravitational binding energy. For $\beta > 0.14$, secular instabilities can develop. For $\beta > 0.27$, dynamical instabilities develop (Fryer, Holz & Hughes 2002). For our slower rotating stars (v5, v20) no instabilities develop. Even

for our fastest spinning cores, the instabilities do not develop until after the collapsed-core mass exceeds $\sim 1\,\mathrm{M_\odot}$. This means that the core forms before instabilities occur and the collapsing core will not fragment. However, for these fastest-spinning models (v200 series), the rotation is sufficient to develop bar modes and gravitational waves from such stars could be detectable out to the Virgo cluster (Fryer et al. 2002).

4 YIELDS: COMPARISON OF AGN STARS TO FIELD STARS

We have shown that the peculiar evolution of AGN-disc stars lead to stellar structures (Section 2) and post-collapse explosion properties (Section 3) that are very different from field stars. The nucleonsynthtetic yields from these stars probe these differences and identify distinguishing features of our AGN stars. In this section, we discuss the yields from our AGN stellar models, contrasting them to supernova yields. We can then compare these yields with the observed abundances in AGN discs. As we shall discuss in Section 5, the observed yields are limited to only a few elements: C, N, O, Ne, Mg, Si, and Fe. For this study, we will focus on these elements. A summary of our calculated yields is shown in Table 3 and Fig. 7.

4.1 Yields from field stars: core-collapse and thermonuclear supernova yields

To compare to our AGN yields, we must first compile the yields from field stars, both core-collapse (CCSN) and thermonuclear (TNSN) supernovae. For core-collapse supernovae, we use the yields from one-dimensional core-collapse calculations using energy deposition to vary the supernova energy (Fryer et al. 2018; Andrews et al. 2020). We focus on the yields from 15, 20, and $25\,\mathrm{M_\odot}$ zero-age main-sequence mass stars with 'normal' core-collapse supernova energies (0.5–3×10^{51} erg). At collapse, these masses are roughly 10.7, 13.0, and $12.3\,\mathrm{M_\odot}$. Table 3 shows a subset of the yields from these models showing the range of yields and, more importantly, yield ratios from these supernovae. Our field star models eject comparable abundances of iron and silicon (Fe/Si ranges from 0.1 to 3 based on progenitor and explosion energy). In our core-collapse supernovae, O dominates the yield, often two orders of magnitude above the yields of Si, Fe, or C. Mg is produced at a factor of a few times lower than C.

Thermonuclear supernovae are major contributors of iron and silicon in the Universe. Because they arise from relatively low-mass progenitors, thermonuclear supernovae should be rare in AGN discs. Stars forming in AGN discs tend to accrete mass even beyond the onset of nuclear burning in the core, driving larger masses. For our field-star distribution, we use a broad sample of thermonuclear supernova calculations from Seitenzahl et al. (2013). These results are based on three-dimensional simulations of deflagration-initiated explosions leading to delayed-detonation explosions. As with most thermonuclear supernovae, they produce large amounts of ^{56}Ni that decays to iron and this iron productions exceeds that of any other element (Fe/Si $\sim$ 1.5–20). These explosions also eject unburned carbon, oxygen, and magnesium from exploding white dwarf. But iron dominates the yields, roughly two orders of magnitude above the Mg and C yields, and more than an order of magnitude greater than the O yield. Alternative explosion mechanisms (e.g. helium detonation or gravitationally confined detonation models) produce the same trends in yield ratios (Seitenzahl & Townsley 2017).

4.2 Yields from our AGN stars

The physics behind the formation and ejection of isotopes in our AGN stars is slightly more complex. It includes three different components: stellar winds, disc winds, and stellar disruption. The stars produced in AGN discs reach very high masses (in excess of $400\,\mathrm{M_\odot}$). First generation stars acquire pristine H and He gas (model v200lowZ) and return CO-laden wind to the disc gas. Later generation star recycle disc gas which has been polluted by their predecessors (model v200). During their main-sequence evolution, a large fraction of the stellar mass is released with He and N abundances enhanced by the CNO burning process (Ali-Dib & Lin 2023). Along their post-main-sequence tracks, the triple-α reaction primarily produces C + O and strong winds eject H, He (typically abundances in field star winds), and heavier elements (with C several times larger than O yields). Since the wind is limited to removing the outer layers, only trace amounts of Ne, Mg, and Si is contained in the ejecta (Table 3).

After the onset of collapse, non-rotating AGN stars contract into black holes and produce no further ejecta. But, if these stars are rotating, a disc is formed that can undergo further burning and drive additional outflows. For these models, we can calculate the ejecta properties from our disc models. The initial ejecta is heated in the disc and we use the disc properties from Popham et al. (1999) to determine the disc temperature. As it moves outward, it shocks the stellar material, heating it. We assume that the wind ejecta quickly blows a jet-like funnel out through the star. We assume the ejecta expands adiabatically, using a simple analytic disc wind model (Kaltenborn et al. 2023).

With these trajectories, we are able to use nuclear network codes to calculate the detailed yields. We post-process the non-interacting disc tracer particles through the NuGrid TPPNP nuclear reaction network (Jones et al. 2015; Pignatari et al. 2016). Each trajectory is integrated in time using a variable-order Bader–Deuflhard integrator (Bader & Deuflhard 1983; Deuflhard 1983; Timmes 1999). Nuclear statistical equilibrium (NSE) is assumed at temperatures above 5 GK and we evolve the electron fraction via a fourth-/fifth-order Cash–Karp type Runge–Kutta integrator (Cash & Karp 1990). For more information on the NuGrid TPPNP code, we refer the reader to Jones et al. (2019b) and Jones et al. (2019a).

The conditions in the disc are typically so hot that the material is, for the most part, in nuclear statistical equilibrium. Most of this material fuses to iron peak elements and remains into Fe as it is ejected. The amount of iron injected into the AGN disc from these outflows depends on the fraction of the disc mass launched in the wind. In Table 3, we assume 20 per cent of the disc mass is lost through disc winds. The disc winds tend to predominantly produce iron peak elements with only trace amounts of the lighter elements.

The outflow from the disc wind will also disrupt the outer envelope of the star as it clears out a funnel ejecting a later-arriving fraction of the stellar material. For our stellar disruption yields, we calculate the stellar material exterior to the black hole when the disc forms and then eject a constant fraction of this exterior profile. For Table 3, we set this fraction to 20 per cent. We assume that the final few days (during silicon burning) do not significantly alter the composition of the ejecta. This final burning phase primarily affects the composition of the innermost part of the star which forms the black hole. Perhaps more importantly, we further assume that the shock of the disc wind propagating through the star does not drive further burning. It is likely that these shocks will drive some burning that will slightly alter the yields from our stellar disruption. The yields from stellar disruption reflect the abundances of the star at collapse, ejecting considerable

Table 3. AGN star and field star ejecta in solar masses. The AGN yields here have contributions from stellar wind, an adiabatically expanding rotation disc wind, and ejecta composed of stellar material due to disruption of the disc wind. The C, N, O yield here do not include their modest changes due to the CNO burning process on the main sequence track. The core-collapse supernova (Fryer et al. 2018; Andrews et al. 2020) and thermonuclear supernova (Seitenzahl et al. 2013) models are used for comparison of final ejecta yields.

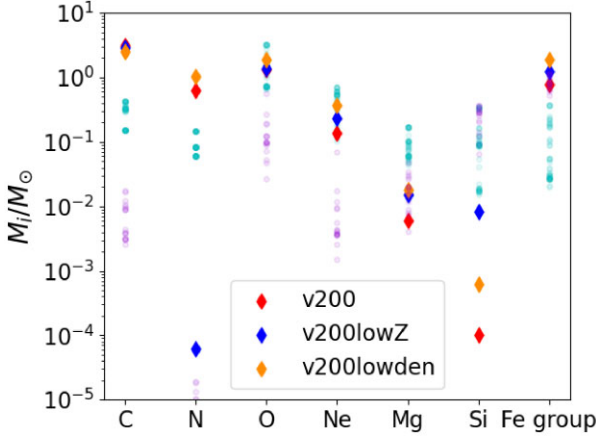| Model	C ($M_\odot$)	N ($M_\odot$)	O ($M_\odot$)	Ne ($M_\odot$)	Mg ($M_\odot$)	Si ($M_\odot$)	Fe peak ($M_\odot$)
Stellar yields							
v200	2.95	0.63	0.86	1.55×10^{-2}	2.70×10^{-5}	4.0×10^{-6}	8.0×10^{-6}
v200lowZ	2.73	6.2×10^{-5}	0.67	1.1×10^{-4}	3.1×10^{-9}	0	0
v200lowden	2.22	1.04	0.75	1.02×10^{-2}	4.4×10^{-5}	7.0×10^{-6}	1.4×10^{-5}
Disc yields							
v200	6.14×10^{-9}	8.50×10^{-13}	1.67×10^{-8}	8.73×10^{-10}	5.01×10^{-10}	1.96×10^{-8}	0.77
v200lowZ	3.52×10^{-8}	7.25×10^{-12}	9.19×10^{-8}	6.70×10^{-9}	3.98×10^{-9}	1.48×10^{-7}	1.23
v200lowden	2.88×10^{-5}	2.55×10^{-11}	1.78×10^{-4}	1.56×10^{-5}	1.57×10^{-5}	2.50×10^{-4}	1.87
Disruption yields							
v200	0.142	0.0	0.476	0.120	0.00589	9.92×10^{-5}	0.0
v200lowZ	0.186	0.0	0.723	0.231	0.0149	0.0084	0.0
v200lowden	0.273	0.0	1.172	0.363	0.0180	0.00036	0.0
Field stars							
Thermonuclear SNe							
N1	0.00261	2.92×10^{-6}	0.0263	0.00153	0.00402	0.0641	1.25
N3	0.00990	9.94×10^{-6}	0.0474	0.00370	0.00736	0.0914	1.17
N5	0.00905	8.47×10^{-6}	0.563	0.00404	0.00875	0.121	1.12
N10	0.00443	3.85×10^{-6}	0.0516	0.00253	0.00789	0.140	1.10
N20	0.00920	8.35×10^{-6}	0.0904	0.00567	0.0149	0.201	0.952
N40	0.00390	4.31×10^{-6}	0.0989	0.00421	0.0156	0.262	0.855
N100H	0.00387	4.26×10^{-6}	0.0730	0.00374	0.0117	0.214	0.961
N100	0.00304	3.21×10^{-6}	0.101	0.00357	0.0154	0.287	0.815
N100L	0.00385	3.98×10^{-6}	0.124	0.00439	0.0185	0.359	0.644
N150	0.0172	1.84×10^{-5}	0.124	0.00920	0.0198	0.275	0.781
N200	0.0121	1.33×10^{-5}	0.196	0.0117	0.0337	0.335	0.643
N300C	0.00886	9.17×10^{-6}	0.121	0.0697	0.0200	0.323	0.720
N1600	0.0106	1.04×10^{-5}	0.191	0.00963	0.0312	0.368	0.608
N1600C	0.0168	1.88×10^{-5}	0.272	0.0176	0.0472	0.353	0.536
N100-0.5	0.00310	1.80×10^{-6}	0.0987	0.00362	0.0203	0.292	0.809
N100-Z0.1	0.00315	4.74×10^{-7}	0.0964	0.00369	0.0269	0.295	0.806
N100-Z0.01	0.00316	1.60×10^{-7}	0.0947	0.00374	0.0290	0.290	0.807
CCSN SNe							
M15bE2.63	0.153	0.060	0.727	0.139	0.059	0.098	0.229
M15bE0.92	0.154	0.060	0.739	0.142	0.060	0.091	0.090
M15bE0.74	0.154	0.060	0.739	0.142	0.060	0.091	0.090
M15aE0.82	0.154	0.060	0.741	0.151	0.062	0.055	0.021
M15aE0.54	0.154	0.060	0.732	0.152	0.062	0.040	0.020
M15aE2.47	0.154	0.060	0.727	0.142	0.059	0.095	0.197
M20cE2.85	0.332	0.083	1.899	0.538	0.103	0.162	0.109
M20cE1.65	0.333	0.083	1.924	0.540	0.103	0.161	0.039
M20cE1.00	0.326	0.083	1.681	0.488	0.094	0.018	0.027
M20cE2.76	0.332	0.083	1.898	0.537	0.103	0.164	0.089
M20aE2.43	0.332	0.083	1.897	0.538	0.103	0.131	0.039
M20bE1.04	0.321	0.083	1.604	0.457	0.088	0.018	0.027
M20aE2.50	0.332	0.083	1.893	0.539	0.104	0.096	0.028
M20aE0.53	0.283	0.083	1.006	0.220	0.048	0.015	0.026
M25aE1.57	0.423	0.146	2.340	0.605	0.125	0.023	0.033
M25d2E2.53	0.422	0.146	3.203	0.615	0.171	0.316	0.053
M25d2E2.64	0.422	0.146	3.203	0.615	0.171	0.316	0.053
M25d2E2.52	0.422	0.146	3.203	0.615	0.171	0.322	0.056
M25d2E2.78	0.422	0.146	3.203	0.615	0.171	0.316	0.053
M25d2E0.75	0.356	0.146	1.075	0.178	0.051	0.017	0.030
M25d3E1.04	0.433	0.146	3.220	0.693	0.170	0.341	0.366

Figure 7. Ejected masses of the elements for all our models. The diamonds represent our different AGN-disc stars. The purple dots correspond to thermonuclear supernovae and the cyan dots represent core-collapse supernovae.

C, O, and Mg. These stars are very different to those of field stars. Fig. 8 shows the stellar abundances of our AGN-disc stars at collapse and those of a typical field star. Our field stars produces nearly 10 times as much Mg as our AGN-disc star. Mg is a sensitive tracer of the C and Ne burning shells and it is not surprising that the Mg abundance is very different in our peculiar AGN disc stars. The high masses of the C/O cores in our AGN disc stars have very different structures than the $15–25\,\mathrm{M_\odot}$ field stars that dominate the nucleosynthetic yields in field stars. If the C/O cores were smaller in our AGN disc stars, the yields from these stars are likely to be more similar to field stars.

Combining all three components of our AGN-disc stars: stellar winds, disc winds, and stellar disruption, we note distinct differences between AGN-disc stars and field star yields. The low C/O ratio of our thermonuclear explosions reflects the conditions of the CO progenitors of these supernovae. A similar ratio is found in the disruptive yields albeit most of the C + O are released before the collapse. Our field star explosions produce Fe on par with Si. Our AGN-disc stars produce no iron unless the star is rotating, but can produce considerable iron if a disc forms.

4.3 abundance ratios

Figs 9, 10, 11, and 12 show the abundance ratios relevant for observations presented here. Let us compare the yields for each of these figures individually. In Fig. 9, we show the C/O versus Si/O ratios. The high mass in our AGN-disc stars produces a large carbon core and much of this carbon is then lost in the stellar winds. The carbon yield in these stellar winds is high, leading to a C/O ratio that is higher than our field star yields. Our AGN-disc models ejected very little Si, leading to a low Si/O ratio. However, our AGN-disc stars may be underestimating the size of the silicon layer (we did not model these stars to collapse). In addition, if the disc wind drives a strong shock, it can also produce considerable Si. Hence, the Si/O ratio may be higher for our AGN-disc models than reported here. We shall revisit the Mg and Si yields with modified stellar models in follow-up investigations.

Fig. 10 shows the O abundance relative to Mg and Si. The high O yield from the winds of our AGN-disc stars and relatively low Mg and Si abundances in the exploding star lead to high O/Mg ratios and low Si/O ratios with respect to supernovae.
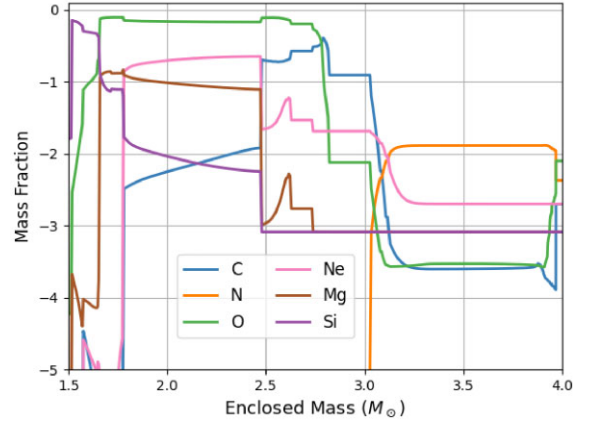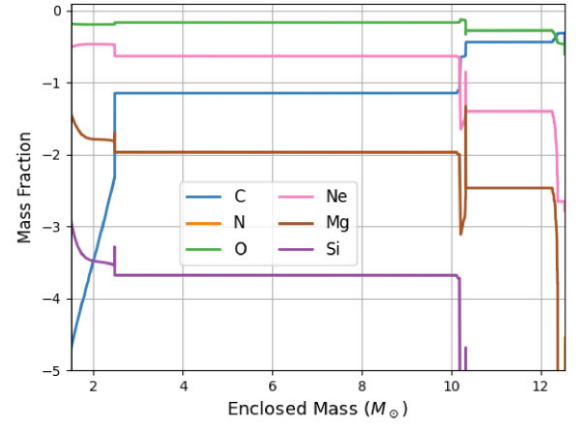

Figure 8. Abundance mass fractions of C, N, O, Ne, Mg, Si versus mass in our v200 AGN-disc star (top) and a $15\,\mathrm{M_\odot}$ field star (bottom). The large C/O core leads to very little variation of the abundances as a function of enclosed mass. Most of the N is destroyed in these stars prior to collapse. There is much more structure in our $15\,\mathrm{M_\odot}$ and that structure leads to very different total Mg and N abundances.
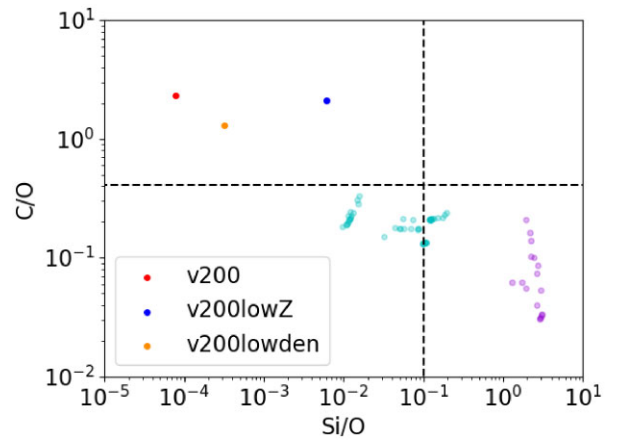

Figure 9. Ejecta ratios of C to O and Si to O for our AGN models (with disc, disruption, and stellar ejecta combined), modest energy core-collapse supernova models (cyan), and thermonuclear supernova models (purple), as compared to solar ratios (black dashed line). We see here that the C/O ratio is significantly higher for our AGN models compared to field stars, while the Si/O ratio is lower than that of the field stars. We also note the Si/O ratio is in good agreement with the expectations from observations seen in Fig. 15 for the low metallicity and, to a lesser extent, the low density model.
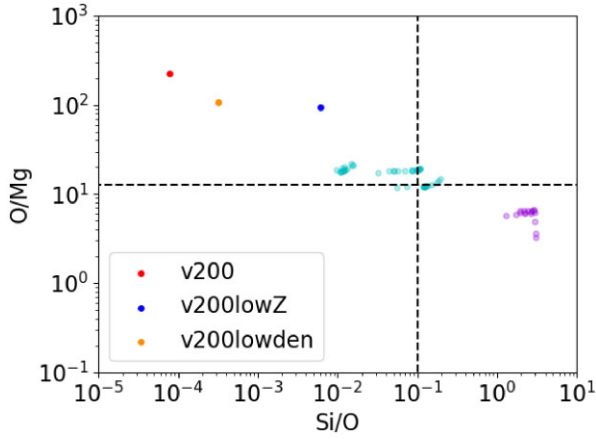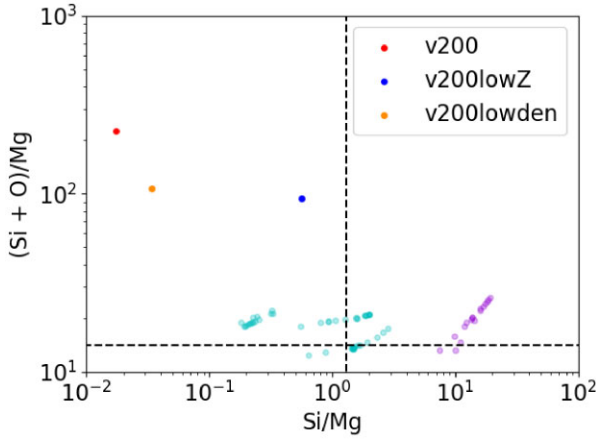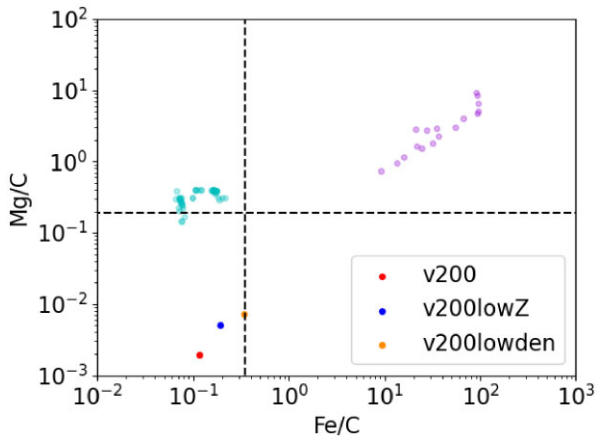
Figure 10. Ejecta ratios of O to Mg and Si to O for our AGN models, modest energy core-collapse supernova models (cyan), and thermonuclear supernova models (purple), as compared to solar ratios (black dashed line).

Figure 11. Ejecta ratios of (Si + O) to Mg and Si to Mg for our AGN models, modest energy core-collapse supernova models (cyan), and thermonuclear supernova models (purple), as compared to solar ratios (black dashed line). Here, we do not see good agreement with Fig. 14 due to our under production of Mg.

Figure 12. Ejecta ratios of Mg and Fe to C for our AGN models, modest energy core-collapse supernova models (cyan), and thermonuclear supernova models (purple), as compared to solar ratios (black dashed line).

Fig. 11 shows the ratios of Si and Si + O to Mg. The low Mg mass fractions in our AGN-disc stars relative to field stars (see Fig. 8) lead to very high (Si + O)/Mg ratios, but the low Si yield leads to Si/Mg ratios that are similar to core-collapse supernovae. With the high Si yields of thermonuclear supernovae, these explosions produce the highest Si/Mg ratios.

Finally, we plot the C ratios with respect to Mg and Fe (Fig. 12). The low Mg production in our AGN-disc stars lead to low Mg/C abundances. But, if the AGN-disc star is rotating, the high Fe production in the disc wind leads to a higher Fe/C ratio than that of normal core-collapse supernovae. Thermonuclear supernovae which dominate Fe production produce the highest Fe/C ratios.

5 YIELDS OBSERVED IN AGN DISCS

By comparing the calculated yields from our AGN disc stars in Section 4 to the observed abundances in AGN discs, we can distinguish between different sources for these nucleosynthetic yields. Ultimately, these yield comparisons can determine the contribution from (and hence rate of) stars formed in AGN discs. But to do so, we must understand the composition of these discs. More importantly, we must understand the uncertainties in these composition measurements.

5.1 Inferring the observed elemental abundances in quasar broad-line region

Previous work has focused on the metallicity in the quasar broad-line region (BLR, in the outskirt of the quasar accretion disc which contains the embedded stars) relative to solar abundance. The indicator (Si IV + O IV])/C IV, as proposed by Nagao, Marconi & Maiolino (006a) provides reliable estimates of BLR abundance. As the overall metallicity increases in the BLR cloud, the fraction of C^{+3} in the cloud decreases almost in inverse proportion to the abundance of heavy elements. This trend reflects the fact that the zone in which C^{+3} dominates gets smaller as the carbon abundance increases. Consequently, as metallicity increases, the intensity of the C IV emission line decreases while that of Si IV increases. Under the assumption that all the α elements' abundance scales with respect to the solar abundance, the inferred BLR mean metallicity of $Z \sim 3Z_\odot$ (e.g. Hamann et al. 2002; Juárez, Maiolino & Mújica 2009). However, to distinguish the stellar population in AGN discs, it is necessary to separately assess the abundance of individual elements.

The difficulty in using line strengths to determine the abundance fractions lies in the fact that the line strengths are determined by the excitation and ionization fractions of the elements. We must apply models determining the line emission that depends on the conditions of the gas and the radiation impinging on this gas. To put some constraints on the abundance of individual elements, we run a set of CLOUDY (Chatzikos et al. 2023) models to study the line intensity ratio for clouds with a slab geometry and the 'Strong Bump' ionizing continuum employed by Nagao et al. (006a). We use a fixed stopping column density of $N_H = 10^{23}$ cm^{-2} (Baldwin et al. 1995), and a wide range of the ionization flux, gas density, which resembles the locally optimally emitting clouds (LOC) for BLR clouds (Baldwin et al. 1995; Korista & Goad 2004). Fig. 13 shows the contour of Mg II/Hβ ratio for a fixed overall metallicity ($Z_\alpha = Z_{Fe} = 3Z_\odot$). For a fiducial BLR gas density of $n_H = 10^{10}$ cm^{-3} (Davidson & Netzer 1979), the line intensity ratio decreases from Mg II/H$\beta \sim 12$ to $\lesssim 1$ when the ionizing flux increases from $\log \phi = 18$ to $\log \phi = 20$ cm^{-2} s^{-1} (corresponding to an increase in the ionization parameter from
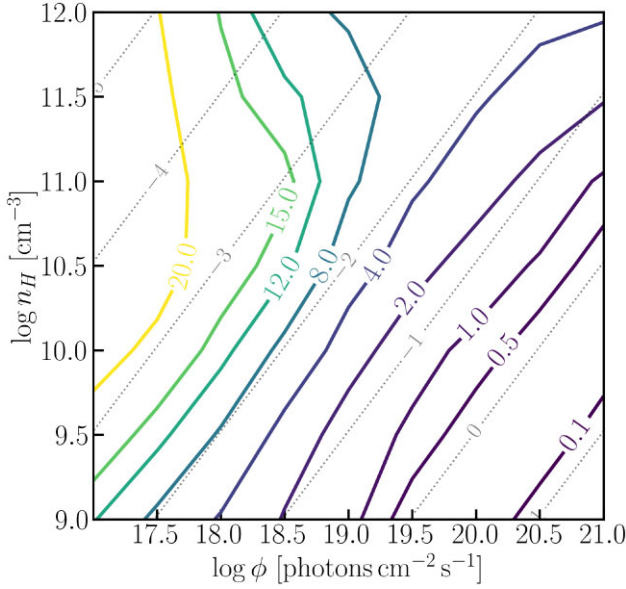
Figure 13. CLOUDY line intensity ratio Mg II/H β for $Z = 3Z_\odot$. The coloured curves correspond to different models with various densities and ionizing flux. The grey dashed contour lines show the corresponding ionization parameter, $U \propto$ ionizing flux/electron number density. This indicates that the intensity of Mg II relative to H β is a strong function U, where Mg II/H β decreases as U increase.

log $U = -2.5$ to log $U = -0.5$, where U is proportional to the ionizing flux divided by the gas density). When U increases, the intensity of ionizing radiation increases, causing a higher fraction of Mg^+ ions to be ionized to Mg^{2+} or higher ionization states. This decrease in the number of Mg^+ ions results in a weaker Mg II emission line, thereby weakening its intensity relative to H β. Our estimates of our abundances will depend on our choices for these properties.

One way to mitigate these uncertainties is to study line ratios. If the excitation and ionization states of lines from different elements are similar, the line ratios would be less sensitive to these conditions. Using element ratios for similar ionization states can reduce the many orders of magnitude uncertainties due to ionizing flux to just a factor of a few. In this section, we will discuss the uncertainties in the measurements and how they affect the abundance ratios for our comparisons shown in Table 4.

To summarize, our goal is to assess the chemical composition of the quasar BLR by matching the typical observed line intensity ratio to the CLOUDY (Chatzikos et al. 2023) model predicted line intensity ratio with model parameters suitable for the quasar BLR (see e.g. Baldwin et al. 1995; Korista & Goad 2004). To further eliminate the uncertainty induced by the variations in metallicity of individual quasars, we take composite SDSS quasars (Vanden Berk et al. 2001; Constantin & Shields 2003) as references for the observed (broad) line ratio for our analysis. We also discuss briefly the extreme values of the observed line intensity ratio among individual quasars to estimate the potential range of abundance ratio that quasar BLR can take.

5.2 Mg to C abundance ratio

The top panel of Fig. 14 compares the observed Mg II/C IV line ratio to the abundance ratio of Mg/C for a wide range of physical parameters ($18 \, \mathrm{cm^{-2} \, s^{-1}} \leq \log \phi \leq 21 \, \mathrm{cm^{-2} \, s^{-1}}$ and $9 \, \mathrm{cm^{-3}} \leq$

Table 4. A summary of the observational constraints on the elemental abundance ratio in the BLR. [A/B] refers to abundance (by number) relative to the solar value. The errors are estimated only based on the observational uncertainties in the BLR emission line ratio. We emphasis that the uncertainties can only be treated as lower limits to the true error budget in the abundance ratio.

Elements	By number	By mass	[A/B]
Mg/C	-0.6 ± 0.1	-0.3 ± 0.1	0.2 ± 0.1
Si/O	-2.4 ± 0.5	-2.2 ± 0.5	-1.2 ± 0.5
C/O	-1.4 ± 0.1	-1.5 ± 0.1	-1.1 ± 0.1
N/O[a]	-0.6	-0.6	-0.2
Fe/Mg[b]	-0.9 ± 0.5	-0.5 ± 0.5	-0.8 ± 0.5
Fe/H	-3.9 ± 0.5	-2.2 ± 0.5	0.6 ± 0.5

[a]The abundances are derived from a separate analysis with the N III]/O III] line intensity ratio in Huang et al. (2023).
[b]Derived by comparing the mean of the observed (Eddington ratio corrected, see Matsuoka et al. 2017) Fe II/Mg II intensity ratio with the model from fig. 10 in Sarkar et al. (2021). The detailed analysis can be found in Huang et al. (2023).

log $n \leq 11 \, \mathrm{cm^{-3}}$). The Mg/C ratio varies by as much as ~ 2 dex for a fixed value of the Mg/C abundance ratio. This further confirms the strong dependence of the line intensity ratio on the ionization parameter, as seen in Fig. 13. As a result, the difference in the Mg II/C IV can be attributed to the sensitivity of the low ionization line Mg II on the ionization parameter, U, as discussed in Section 5. A similar argument applies to the C IV intensity relative the H β, where the C IV gets stronger relative to H β when U increases. The LOC model, on the other hand, potentially resolves the problem that both Mg II and C IV are sensitive to the ionization parameter. The LOC average, weighted by uniform H β flux, is shown as the dash–dotted ($-2.0 < U < 0$) and solid ($-3.5 < U < -1.5$). We focus on the narrower range of ionization parameter where $-2.0 < U < 0$ that brackets the physical parameter that better reproduces the bulk of the BLR spectrum. The observed line ratio, as indicated by the shaded orange region, is from the Vanden Berk et al. (2001) quasar composite spectrum. The intersection between the LOC average (dash–dotted line) and the observed line ratio suggests that the Mg/C abundance ratio is around -0.6 by number (or -0.3 by mass). Given the large variation in the abundance ratio due to the variation in the ionization stage, we only attempt to estimate the lower limit for the error budget, which is given by the observed uncertainties in the emission line ratio.

5.3 Si to O abundance ratio

Huang et al. (2023) showed that although the ratio (Si IV + O IV])/C IV can be served as a metallicity indicator for the BLR, the individual abundance ratio (e.g. Si and O) cannot be easily determined form (Si IV + O IV])/C IV ratio alone. In an attempt to disentangle the dependence on the (Si IV + O IV])/C IV ratio on the overall metallicity versus the individual abundance ratio, we run a set of CLOUDY models with varying the Si/O ratio and fixed overall metallicity with $Z = 3Z_\odot$. We use the Si IV/O IV] line ratio as the tracer of Si/O abundance ratio. The Si IV is usually blended with O IV] which contributes extra uncertainties to the observed line ratio. Therefore, we look at Narrow-Line Seyfert 1 galaxies (NLS1), which typically exhibit narrow emission lines with FWHM(H β) $\lesssim 2000 \, \mathrm{km \, s^{-1}}$ (Osterbrock & Pogge 1985). The bottom panel of Fig. 14 shows the observed Si IV/O IV] line intensity ratio from Constantin & Shields (2003) NLS1 composite spectrum. The LOC average intercepts with the observed value implies that the Si/O ratio varies from -2.9 to
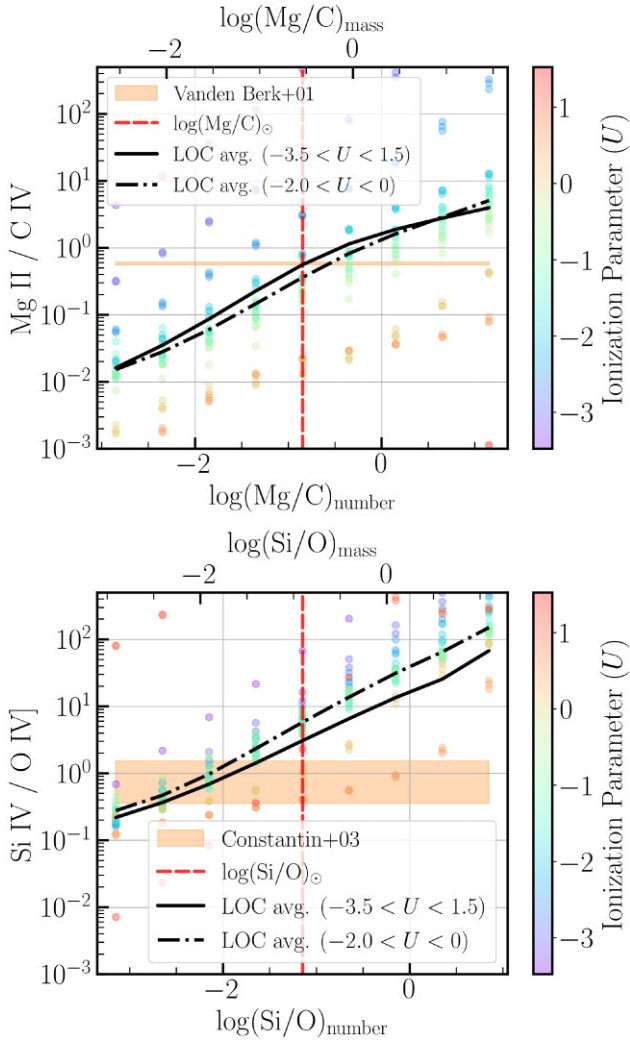
Figure 14. Top panel: CLOUDY line intensity ratio Mg II/C IV for $Z = 3Z_\odot$. The scatter shows Mg II/C IV for each of the grid pairs with $18\,\mathrm{cm}^{-2}\,\mathrm{s}^{-1} \leq \log\phi \leq 21\,\mathrm{cm}^{-2}\,\mathrm{s}^{-1}$ and $9\,\mathrm{cm}^{-3} \leq \log n_\mathrm{H} \leq 11\,\mathrm{cm}^{-3}$. The solid black curve marks the LOC average for Mg II/C IV over the full range of the ionization parameter ($-3.5 < U < 1.5$), weighted by the Hβ flux. The dotted black line shows the same line ratio, but averaged over a more realistic range of the ionization parameter for the BLR ($-2.0 < U < 0$). The red dashed line indicates the solar value of [Mg/C]. The observed Mg II/C IV ratio is ~ 0.58 (Vanden Berk et al. 2001), as indicated by the horizontal dashed line. Bottom panel: CLOUDY line intensity Si IV/O IV] ratio for $Z = 3Z_\odot$. The orange shaded region shows the observed Si IV/O IV] line intensity ratio in the (Constantin & Shields 2003) composite spectrum for the NLS1.

-1.9. A similar result is given by realistic values of the ionization parameter ($-2.0 < U < 0$), where Si/O ratio varies from -2.7 to -1.7. The O IV] line has critical density of $n_\mathrm{crit} = 1.12 \times 10^{11}\,\mathrm{cm}^{-3}$ (Hamann et al. 2002), so it is less affected by the collisional de-excitation at high density (the highest density in our CLOUDY model grid has $\log n_\mathrm{H} = 11\,\mathrm{cm}^{-3}$). In addition, the shape of the ionizing continuum from Nagao et al. (006a) may not accurately represent the ionizing continuum for the NLS1, due to the fact that the NLS1 galaxies typically have high Eddington ratio (Boroson & Green 1992). Fig. 1 in Ferland et al. (2020) shows the ionizing spectral energy distribution (SED) for AGNs with varying Eddington ratios. The peak of the ionizing continuum shifts to higher energy as we move the Eddington ratio, indicating a harder SED in the range of
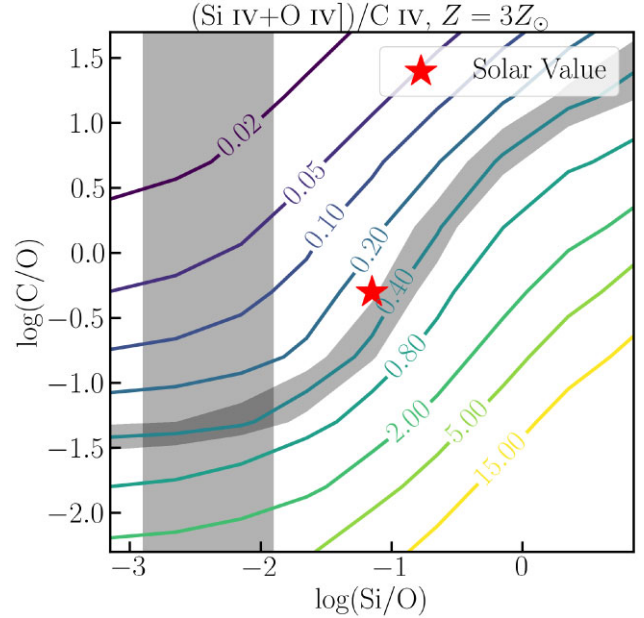
Figure 15. CLOUDY line intensity ratio (Si IV + O IV])/C IV as a function of log(C/O) and log(Si/O) abundance ratio by number for $Z = 3Z_\odot$. The vertical grey shaded region marks the expected Si/O ratio [log(Si/O) = -2.9 to -1.9 by number] from comparing the observed Si IV/O IV] intensity ratio in (Constantin & Shields 2003) and that of the CLOUDY LOC model (See Fig. 14). The grey shaded region following the contour line centred at 0.40 marks the typical observed (Si IV + O IV])/C IV ratio from SDSS quasar composite (Vanden Berk et al. 2001). By construction, the intersection of the two shaded region marks the range of the inferred C/O abundance ratio, from -1.5 to -1.3. The solar abundance ratio is marked as red star.

~ 30–55 eV, which brackets the ionizing potential of Si IV and O IV], respectively. A direct consequence of the SED dependence on the Eddington ratio is that our LOC model average of Si IV/O IV] will get smaller if the bulk of the NLS1 galaxies have high Eddington ratio, therefore the inferred Si/O ratio will be higher. A final caveat for the estimation is the assumption that the underlying abundance for α-elements is $Z = 3Z_\odot$. This is a valid assumption based on previous studies on the BLR matellicity. However, the estimation of individual abundance ratio can be affected by the baseline abundance for α-elements. To this end, we run the CLOUDY models with the same setup but with $Z = Z_\odot$, we find the difference between the inferred Si/O ratio to be small between $Z = Z_\odot$ and $Z = 3Z_\odot$.

As an attempt to utilize the inferred Si/O abundance to find the range of C/O abundance, we run CLOUDY model for the (Si IV + O IV])/C IV ratio as a function of both C/O and Si/O abundance ratio by number, where O and other α-element abundance is kept at (O/H) = 3(O/H)$_\odot$. The result is shown in Fig. 15. The vertical grey shaded region shows the value of the inferred Si/O abundance, and the shaded region following the shape of the contour at (Si IV + O IV])/C IV ~ 0.4 marks the typical value of the observed (Si IV + O IV])/C IV ratio.

5.4 Constraints on the Fe/Mg and Fe/H abundance ratio

Studies of the iron abundance in the BLR and its redshift dependence have largely focused on the ultraviolet Fe II/Mg II ratio. The Mg II$\lambda 2800$ line and the UV Fe II bands around 2400 Å are close in wavelength and involve similar stages of ionization. These studies generally find that Fe II/Mg II depends little, if at all, on
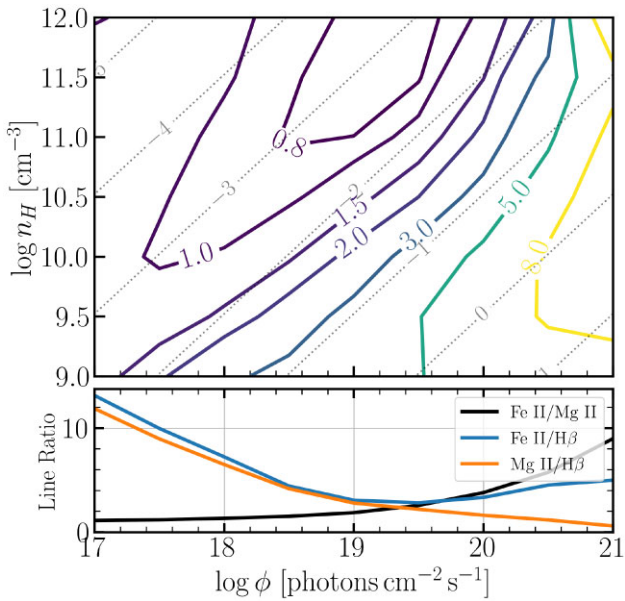
Figure 16. *Top*: Line intensity ratio Fe II/Mg II for $Z_\alpha = Z_\odot$, with a solar iron abundance. The curves correspond to different models with various densities and ionizing flux. The dashed contour lines show the corresponding ionization parameter, U. To first order, the Fe II/Mg II contour lines follow closely to the contour lines of the ionization parameter. This can be partially explained with the U dependence of the Mg II line equivalent width. As indicated in Fig. 13, the Mg II/Hβ decreases as U increase. *Bottom*: line ratio Fe II/Mg II, Fe II(UV)/Hβ, and Mg II/Hβ as a function of ionizing flux. To compute the average line ratio, we assume the weight in density is uniform in $\log n_H$, in other words, $w(n_H) \propto n_H^{-1}$ (Baldwin et al. 1995; Korista & Goad 2004). This demonstrates the sensitivity of the Fe II/Mg II on the ionization flux even for a fixed [Fe/Mg] abundance ratio.

redshift (Maiolino et al. 2003; Verner et al. 2009; De Rosa et al. 2011; Schindler et al. 2020; Yang et al. 2021; Wang et al. 2022). However, caution is warranted for several reasons. For example, the Fe II/Mg II intensity ratio cannot be treated as the effect of changing iron abundance alone. As indicated on the bottom panel of Fig. 16, with a fixed solar Fe/Mg abundance ratio, the average Fe II/Mg II intensity ratio, weighted by n_H^{-1}, increases from 1.0 to 8.8 as the ionizing flux increases from $\log \phi = 17$ to 21 cm^{-2} s^{-1}. In contrast, for a single zone model ($\log n_H = 11$ cm^{-3}, $\log \phi = 20$ cm^{-2} s^{-1}, and $v_{turb} = 100$ km s^{-1}), Fe II/Mg II line intensity only goes as (Fe/Mg)$^{0.2}$ (Sarkar et al. 2021). Such a weak dependence of iron emission on the iron abundance implies that the uncertainty of the inferred ratio is large. As shown in Table 4, we assign the uncertainty in [Fe/Mg] and [Fe/H] to ±0.5 only to encompass the variation in the observed line intensity ratio. If we include the uncertainty from different modelling parameters, the actual uncertainty can only be larger.

The Mg abundance in stars and stellar explosions can very dramatically with the stellar structure and explosion energies (Maeder & Meynet 2010; Fryer et al. 2018). Until we have run a suite of stellar models and explosive yields to determine the full range of results from our models, the Fe/Mg inferred from Fe II/Mg II may be biased by our particular small set of simulations. A potential solution is to inspect the Fe/H abundance directly from the optical Fe II emission and its intensity relative to the Hβ. It is worth to emphasize that many caveats arises from such an attempt:

(1) It has been well established that there exist empirical correlations between the optical Fe II emission and fundamental AGN properties such as the SMBH mass, the Eddington ratio, the radio loudness or the X-ray properties. For example, the equivalent width ratio between optical Fe II and Hβ [e.g. $R_{FeII} = EW(Fe II)/EW(H\beta)$ where EW(Fe II) is the equivalent width of the optical blend Fe IIλ4434–4684] correlates with the width of the line FWHM (Hβ) as well as the equivalent width of [O III]. This correlation is known as the eigenvector 1 (EV1) (Boroson & Green 1992; Sulentic, Marziani & Dultzin-Hacyan 2000). Similar to Fe II/Mg II discussed above, the large variation in Fe II/Hβ across objects cannot be explained by the difference in the Fe/H abundance alone. Moreover, among some changing look AGN candidates, R_{FeII} changes as the underlying continuum changes (Gaskell et al. 2022). Petrushevska et al. (2023) presented an changing look NLS1 where R_{FeII} decreases by a factor of two in ~ 2000 d of monitoring. A comprehensive study by Panda (2022) demonstrates that the variation in the ionizing SED, together with the location where Fe II emission is produced, can affect the intensity of the iron emission.

(2) Several results from reverberation mapping have shown that the optical Fe II emission originates in a larger radius than the typical radius of the BLR. For example, Barth et al. (2013) find that the centroid of the cross-correlation function between Fe II and V-band light curve is ~ 1.5–2 times larger than that of the Hβ line. This is further confirmed by the comprehensive analysis of the Fe II emitting region in Gaskell et al. (2022). This raises the question whether we can use a one-zone model (i.e. a fixed ionizing flux and gas density) to explain the observed Fe II/Hβ ratio?

(3) As a consequence, a larger radius where optical Fe II is emitted indicates that Fe II emission is be more affected by the condensation into grains. As discussed in Shields, Ludwig & Salviander (2010), the depletions of Fe can be as large as two orders of magnitude; therefore, the abundance of Fe of the gas phase Fe abundance that we observe may not reflect the true Fe/H of the BLR gas. Our estimates can only be treated as lower limits of the true Fe abundance in the BLR.

To mitigate the above uncertainties, we propose to infer a range of possible Fe/H abundance that can help us to constrain the stellar evolution yield without trying to disentangle the physical properties that causes the variations between the optical Fe II emission among objects. Fig. 17 shows the Fe IIλ4570 blend/Hβ line intensity ratio contour as a function of density and ionizing flux for $Z_\alpha = Z_\odot$ and hydrogen column density $\log N_H = 25$ cm^{-2}. For a fixed ionizing SED and iron abundance [Fe/H] = 1, the Fe II/Hβ ratio varies from ~ 0.1 to 1.2 depending on the ionization parameter. The typical physical condition of the optical Fe II emitting region, $\log n_H = 11$ cm^{-3}, $\log \phi = 20.5$ cm^{-2} s^{-1}, $U = -1$ (Zhang et al. 2024), is marked as red cross in Fig. 17. This single-zone model gives a Fe II/Hβ of 0.75. As a reference, the typical observed Fe II/Hβ ratio is ~ 0.5, with a large variation depending on the quasar population, ranging from ~ 0.1 to > 1.5. (e.g. Boroson & Green 1992; Shen & Ho 2014; Marziani et al. 2018). For extreme iron emitting object such as I Zw 1, a NLS1 galaxy with Fe II/Hβ (Persson 1988; Véron-Cetty, Joly & Véron 2004), Fe II/H$\beta \sim 1.76$, the inferred iron abundance may be extreme as well, if the strong Fe II/Hβ could be caused by enhancement in high metallicity (Floris et al. 2024), hence high [Fe/H]. On the other hand, recent discoveries of *JWST* high-redshift, low-luminosity ($\log L_{H\beta} \lesssim 44$ erg s^{-1}) broad-line AGNs show weak optical Fe II emission relative to Hβ(e.g. Trefoloni et al. 2024, and references therein). This can be explained by the low metallicity in the BLR or the depletion of Fe into grains (Shields et al. 2010; Trefoloni et al. 2024). Despite the extreme iron emitting objects, a supersolar iron abundance ([Fe/H] $\gtrsim 0.6$) is needed to explain the typical observed Fe II/Hβ ratio.
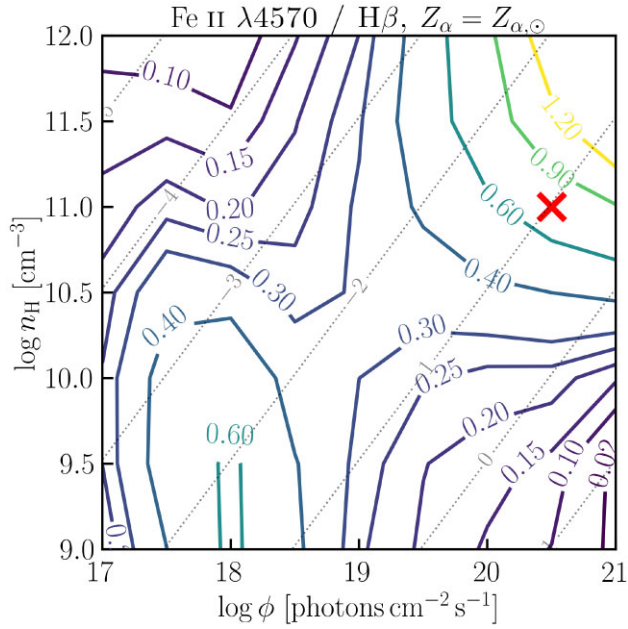
Figure 17. *Top*: Line intensity ratio Fe IIλ4570 blend/Hβ for $Z_\alpha = Z_\odot$ and hydrogen column density $\log N_H = 25$ cm^{-2}, with supersolar iron abundance, (Fe/H) = 10(Fe/H)$_\odot$ by number. The contour curves correspond to different models with various densities and ionizing flux. The dashed contour lines show the corresponding ionization parameter, U. The cross marks the typical physical conditions ($\log n_H = 11$ cm^{-3}, $\log \phi = 20.5$ cm^{-2} s^{-1}, $U = -1$) for the optical Fe II-emitting region (Zhang et al. 2024). Clear enhancement in the predicted Fe II/Hβ is seen towards high hydrogen density and large ionization flux (top-right of the contour plot).

5.5 Abundance comparison

Our fiducial AGN-star model produces $\sim 3\,M_\odot$ of C and O as well as $\sim 1\,M_\odot$ of N and Fe yield (Table 3). As we have indicated above, in lieu of the independent abundance determination for individual elements from AGNs' broad emission lines, we rely on the evaluation of their relative abundance and infer their abundance under the assumption of O abundance being three times the solar value (Section 5.3). Table 4 summarizes the observed abundance ratios and their uncertainties from this study. Table 5 compares the observed element ratios (by mass) to the ranges predicted in our AGN-disc stars, field CCSN and field TNSN models. The observed abundance ratios are fairly well fitted by the field CCSN models. The only discrepancy with the observed values is the C/O ratio from CCSN models being too high and the N/O ratio being too low.

For the AGN stars, the observed N/O is much larger than that for the pristine v200lowZ model but comparable to that for the v200 model.

This difference supports the assumption that the N yield mostly comes from second or later-generation stars. In comparison with observation, our fiducial model overpredict C/O and underpredict Mg/O by more than an order of magnitude. If these fiducial models are correct, the high C/O ratio from AGN disc stars would place strong limits on the yield contributions from these stars. But it is worth noting that the Fe/O of the AGN-disc stars is larger than the observationally inferred value and that produced by CCSN. Such high Fe yield is more than adequate to explain the large iron abundance fractions ([Fe/H] $\gtrsim$ 0.6) at high redshifts (prior to contributions from TNSN).

6 SUMMARY AND DISCUSSIONS

Massive stars form in AGN discs. The continued accretion on to these stars after formation leads to a very different evolutionary pathways than normal field stars. This different evolutionary history also produces stars whose structures at collapse differ greatly from field stars of the same collapse mass. The main objective of this paper is to determine the heavy-element (especially Fe) yield from these stars. These quantities provide observable diagnostics for AGN discs' structure and place constraints on the population of remnant stellar mass black holes contained within them.

In a previous analysis of this process (Ali-Dib & Lin 2023), we have already showed that (1) C + O are generated through triple-α reaction and released during the post-main-sequence evolution of all AGN stars, including the first generation stars, (2) He and N are enriched through CNO burning and their yields are released during the main-sequence evolution of second or later-generation AGN stars, and (3) although modest amounts of Mg, Si, and Fe are generated though the α-chain process on the post-main-sequence track, they are confined deeply in the core and very little fractions are released into the AGN disc.

Due to technical limitations, these MESA calculations end at the onset of Si burning. The residual cores are expected to further deplete the Mg, Si, and enhance Fe contents before they undergo gravitational collapse. With negligible spin angular momentum, the subsequent collapse of the cores with large residual mass ($\sim 12\,M_\odot$ in the fiducial model) leads to the formation of stellar mass black holes without supernovae and significant amount of Mg, Si, and Fe yields. However, accretion on to these post-main-sequence AGN stars causes them to rotate. With a modest amount of angular momentum (corresponds to ~ 0.1 the core's break up speed), a significant mass fraction of the collapsing core forms a disc around a recently formed central black hole. In this paper, we show that these discs generate jet-driven explosions that produce large amounts of iron-peak elements and release ($\sim 1\,M_\odot$) Fe yield into the AGN disc. Moreover the disc wind intercepts the delayed infall of the dwindling outer regions of

Table 5. Comparison of abundance ratios by mass. The observed abundance ratio is estimated by matching the observed line intensity ratio in the quasar BLR to the CLOUDY model predicted line intensity ratio (see Section 5).

Element ratio	Observed	AGN-disc	CCSN	TNSN	Solar value
Mg/C	-0.3 ± 0.1	< -2.0	-1.0 to -0.4	-0.1 to 1.0	-0.55
Si/O	-2.2 ± 0.5	< -2.0	-2.0 to -1.0	-0.7 to -0.5	-0.91
C/O	-1.5 ± 0.1	$0.0–0.4$	-0.8 to -0.2	$-1.5 - -0.7$	-0.43
N/O	-0.6	$-4.0 - 2.0$	$-2.0 - -1.2$	$-6.0 - -5.0$	-0.82
Fe/Mg	-0.5 ± 0.5	~ 2	$-1 - 0.6$	$1.0 - 2.5$	0.28
Fe/O[a]	-0.4 ± 0.5	$-0.2 - 0.0$	$-1.9 - -0.5$	$0.3 - 1.7$	-0.69

[a]For better comparison with the modelled Fe yield, the abundance ratio (Fe/O) is estimated by scaling the observed (Fe/H) ratio (see Table 4) based on the assumption that (O/H) = 3(O/H)$_\odot$ by number.

the collapsing cores. This interruption further modifies the abundance and ejects modest amounts of Mg and Si yields.

With these collapse/explosion models, we are able to estimate the nucleosynthetic yields from AGN disc stars. The yields are comprised of stellar wind ejecta prior to collapse, disc wind ejecta after the formation of a black hole and stellar disruption as the disc wind and disc jet plow through the star. These models show that, with expected rotation rates of these stars, discs form around the newly collapsed stellar mass black holes. High temperatures in these discs lead to the prolific production of iron. A primary result of this study is our demonstration that the winds from these discs can inject considerable amounts of iron into the AGN disc.

The full nucleosynthetic yields from these fiducial models have very different signatures from those of field stars. Although our results generally support the proposition that the He, C, N, O, Si, and Fe abundance inferred from AGN's broad emission lines can be qualitatively attributed to the yields from embedded disc stars, they underpredict Mg/O and overpredict C/O by about an order of magnitude from, while the Si/O ratio remains within the range of observationally inferred values (Table 5).

However, both the theoretical results and the observational interpretations are still preliminary. Our set of AGN-disc stellar (the fiducial) models uses a narrow prescription for mass accretion and subsequent mass-loss. But AGN stars form and evolve at distances ranging from $\sim 10^{-2}$ pc to a few pc from the SMBH, where the boundary conditions vary significantly. The disc properties in our study are appropriate for luminous AGNs, including quasars. Indeed, the supersolar metallicity of the BLR has been inferred from AGNs with a range of 'Eddington ratios' and it has no established dependence on the SMBHs' mass or on their Eddington ratio. The presence of a population of young (S and disc) stars near Sgr A∗ (with a mass of $4 \times 10^6 \, M_\odot$) is very suggestive that in situ star formation commonly take place around AGNs with modest mass and accretion rates as well.

None the less, in follow-up studies, we plan to (1) examine the model dependence on various parameters including the background density and sound speed of the AGN disc to determine the dependence on the disc properties and (2) modify the prescription for the radiation-pressure feedback on the accretion flow to study the dependence on our chosen mass-loss model. These investigations are likely to produce a broader suite of stellar models. The rates of nucleosynthesis at various stages of AGN-stars' evolution are affected by their masses and therefore their mass accretion and wind-loss rates.

We employed a simplified model for the explosions produced from the stellar collapse model, focusing primarily on a parametrized mass-loss. Future work will study the energy ejection from jets and this wind mass-loss and their role in driving explosive nucleosynthesis model to achieve more accurate yield and range of yield estimates. This physics is currently poorly understood and future work, guiding by current simulations, will mostly focus on placing bounds on these yields. Finally, in order to determine the implied abundance distribution over entire AGN discs, we also need to take into account the injection, accumulation, and diffusion of heavy elements at different AGN-disc radii.

On the observational side, the abundance ratios for individual elements with respect to O (Section 5) includes all α-elements (with assumed solar abundance distribution and three times the solar values), excluding those particular species. These determinations can be improved with self-consistent CLOUDY models without the assumption of solar abundance distribution. It is also useful to examine the time-dependent line-ratio variations among changing-look

and rapidly varying AGNs to separate the abundance contribution from the emission-line physics. These steps are the natural extension of our quest to place more-reliable quantitative constraints on the contribution from AGN-disc stars and to set limits on the formation rates of AGN stars and embedded black holes.

DATA AVAILABILITY

The data underlying this article will be shared on reasonable request to the corresponding author.

REFERENCES

Abbott B. P. et al., 2019, Phys. Rev. X, 9, 031040
Abbott R. et al., 2021, Phys. Rev. X, 11, 021053
Abbott R. et al., 2023, Phys. Rev. X, 13, 041039
Abbott R. et al., 2024, Phys. Rev. D, 109, 022001
Ali-Dib M., Lin D. N. C., 2023, MNRAS, 526, 5824
Andrews S., Fryer C., Even W., Jones S., Pignatari M., 2020, ApJ, 890, 35
Arca Sedda M., Naoz S., Kocsis B., 2023, Universe, 9, 138
Artymowicz P., Lin D. N. C., Wampler E. J., 1993, ApJ, 409, 592
Bader G., Deuflhard P., 1983, Numer. Math. (Heidelb.), 41, 373
Baldwin J., Ferland G., Korista K., Verner D., 1995, ApJ, 455, L119
Barth A. J. et al., 2013, ApJ, 769, 128
Belczyński K., Bulik T., Zbijewski W., 2000, A&A, 355, 479
Belczynski K. et al., 2020, A&A, 636, A104
Boroson T. A., Green R. F., 1992, ApJS, 80, 109
Britt D., Johanson B., Wood L., Miller M. C., Michaely E., 2021, MNRAS, 505, 3844
Broekgaarden F. S. et al., 2021, MNRAS, 508, 5028
Cantiello M., Jermyn A. S., Lin D. N. C., 2021, ApJ, 910, 94
Cash J. R., Karp A. H., 1990, ACM Trans. Math. Softw., 16, 201
Chatzikos M. et al., 2023, RMxAA, 59, 327
Chen Y.-X., Lin D. N. C., 2023, MNRAS, 522, 319
Chen Y.-X., Lin D. N. C., 2024, ApJ, 967, 88
Chen Y.-X., Jiang Y.-F., Goodman J., Ostriker E. C., 2023, ApJ, 948, 120
Chen Y.-X., Jiang Y.-F., Goodman J., Lin D. N. C., 2024, ApJ, 974, 106
Constantin A., Shields J. C., 2003, PASP, 115, 592
Davidson K., Netzer H., 1979, Rev. Mod. Phys., 51, 715
Davies M. B., Lin D. N. C., 2020, MNRAS, 498, 3452
De Rosa G., Decarli R., Walter F., Fan X., Jiang L., Kurk J., Pasquali A., Rix H. W., 2011, ApJ, 739, 56
Deng H., Mayer L., Latter H., 2020, ApJ, 891, 154
Deuflhard P., 1983, Numer. Math. (Heidelb.), 41, 399
Eldridge J. J., Stanway E. R., 2016, MNRAS, 462, 3302
Ferland G. J., Done C., Jin C., Landt H., Ward M. J., 2020, MNRAS, 494, 5917
Floris A., Marziani P., Panda S., Sniegowska M., D'Onofrio M., Deconto-Machado A., del Olmo A., Czerny B., 2024, A&A, 689, A321
Fryer C. L., Benz W., Herant M., 1996, ApJ, 460, 801
Fryer C. L., Woosley S. E., Hartmann D. H., 1999, ApJ, 526, 152

Fryer C. L., Holz D. E., Hughes S. A., 2002, ApJ, 565, 430

Fryer C. L., Belczynski K., Wiktorowicz G., Dominik M., Kalogera V., Holz D. E., 2012, ApJ, 749, 91

Fryer C. L., Andrews S., Even W., Heger A., Safi-Harb S., 2018, ApJ, 856, 63

Fryer C. L., Olejak A., Belczynski K., 2022, ApJ, 931, 94

Gaskell M., Thakur N., Tian B., Saravanan A., 2022, Astron. Nachr., 343, e210112

Goodman J., 2003, MNRAS, 339, 937

Goodman J., Tan J. C., 2004, ApJ, 608, 108

Gottlieb O., Jacquemin-Ide J., Lowell B., Tchekhovskoy A., Ramirez-Ruiz E., 2023, ApJ, 952, L32

Hamann F., Korista K. T., Ferland G. J., Warner C., Baldwin J., 2002, ApJ, 564, 592

Harris C. R. et al., 2020, Nature, 585, 357

Heger A., Fryer C. L., Woosley S. E., Langer N., Hartmann D. H., 2003, ApJ, 591, 288

Huang J., Lin D. N. C., Shields G., 2023, MNRAS, 525, 5702

Hunter J. D., 2007, Comput. Sci. Eng., 9, 90

Jermyn A. S., Dittmann A. J., McKernan B., Ford K. E. S., Cantiello M., 2022, ApJ, 929, 133

Jones S., Hirschi R., Pignatari M., Heger A., Georgy C., Nishimura N., Fryer C., Herwig F., 2015, MNRAS, 447, 3115

Jones S. W. et al., 2019a, MNRAS, 485, 4287

Jones S. et al., 2019b, A&A, 622, A74

Juárez Y., Maiolino R., Mújica R., 2009, in Recillas E., Luna A., Mayya Y. D., eds, Revista Mexicana de Astronomia y Astrofisica Conference Series. Huatulco, Oxoaca, p. 163

Kaltenborn M. A. R., Fryer C. L., Wollaeger R. T., Belczynski K., Even W., Kouveliotou C., 2023, ApJ, 956, 71

Korista K. T., Goad M. R., 2004, ApJ, 606, 749

Kritos K., Strokov V., Baibhav V., Berti E., 2024, Phys. Rev. D, 110, 043023

Kruckow M. U., Tauris T. M., Langer N., Kramer M., Izzard R. G., 2018, MNRAS, 481, 1908

MacFadyen A. I., Woosley S. E., 1999, ApJ, 524, 262

McKernan B., Ford K. E. S., 2024, MNRAS, 531, 3479

MacLeod M., Lin D. N. C., 2020, ApJ, 889, 94

Maeder A., Meynet G., 2010, New Astron. Rev., 54, 32

Maiolino R., Juarez Y., Mujica R., Nagar N. M., Oliva E., 2003, ApJ, 596, L155

Mandel I., Broekgaarden F. S., 2022, Living Rev. Relativ., 25, 1

Marziani P. et al., 2018, Front. Astron. Space Sci., 5, 6

Matsuoka K., Nagao T., Maiolino R., Marconi A., Park D., Taniguchi Y., 2017, A&A, 608, A90

Nagao T., Marconi A., Maiolino R., 2006a, A&A, 447, 157

Osterbrock D. E., Pogge R. W., 1985, ApJ, 297, 166

Paczynski B., 1978, Acta Astron., 28, 91

Panda S., 2022, Front. Astron. Space Sci., 9, 850409

Paxton B. et al., 2013, ApJS, 208, 4

Persson S. E., 1988, ApJ, 330, 751

Petrushevska T. et al., 2023, A&A, 669, A140

Pignatari M. et al., 2016, ApJS, 225, 24

Popham R., Woosley S. E., Fryer C., 1999, ApJ, 518, 356

Rastello S., Mapelli M., Di Carlo U. N., Giacobbo N., Santoliquido F., Spera M., Ballone A., Iorio G., 2020, MNRAS, 497, 1563

Rodriguez C. L., Chatterjee S., Rasio F. A., 2016, Phys. Rev. D, 93, 084029

Romagnolo A., Belczynski K., Klencki J., Agrawal P., Shenar T., Szécsi D., 2023, MNRAS, 525, 706

Sarkar A. et al., 2021, ApJ, 907, 12

Schindler J.-T. et al., 2020, ApJ, 905, 51

Seitenzahl I. R., Townsley D. M., 2017, in Alsabti A. W., Murdin P., eds, Handbook of Supernovae. Springer International Publishing, New York, NY, p. 1955

Seitenzahl I. R. et al., 2013, MNRAS, 429, 1156

Shakura N. I., Sunyaev R. A., 1973, A&A, 500, 33

Shen Y., Ho L. C., 2014, Nature, 513, 210

Shields G. A., Ludwig R. R., Salviander S., 2010, ApJ, 721, 1835

Stevenson S., Clarke T. A., 2022, MNRAS, 517, 4034

Sulentic J. W., Marziani P., Dultzin-Hacyan D., 2000, ARA&A, 38, 521

Thompson T. A., Quataert E., Murray N., 2005, ApJ, 630, 167

Timmes F. X., 1999, ApJS, 124, 241

Trefoloni B. et al., 2024, preprint (arXiv:2410.21867)

Vanden Berk D. E. et al., 2001, AJ, 122, 549

Verner E., Bruhweiler F., Johansson S., Peterson B., 2009, Phys. Scr., 134, 014006

Véron-Cetty M. P., Joly M., Véron P., 2004, A&A, 417, 515

Wang S. et al., 2022, ApJ, 925, 121

Yang Y. et al., 2019, Phys. Rev. Lett., 123, 181101

Yang J. et al., 2021, ApJ, 923, 262

Zevin M. et al., 2021, ApJ, 910, 152

Zhang X., Wang T., Gary F., He Z., Wang Y., 2024, ApJ, 971, 6

This paper has been typeset from a TeX/LaTeX file prepared by the author.